POLYOXOMETALATES

Open Access
RESEARCH ARTICLE

Block polymer-modified molybdenum phosphide based on carbon nitride nanosheets for efficient hydrogen evolution

Jiao Li[1], Zhennan Liu[1], Chengwu Wang[1], Tiancong Shi[2], Xuejian Zhang[1] ✉, Xiao Li[2] ✉, Huisheng Liu[1], Yongtao Li[1], and Zhongmin Su[2] ✉

[1] *School of Materials Science and Engineering, Jilin Jianzhu University, Changchun 130018, China*
[2] *School of Chemical and Environmental Engineering, Changchun University of Science and Technology, Changchun 130022, China*

Cite This: *Polyoxometalates*, **2026**, *5*, 9140115

Read Online

ABSTRACT: The development of nonprecious metals and green hydrogen evolution reaction (HER) electrocatalysts is a major research focus in the context of a two-carbon strategy. In this study, we synthesized a high-efficiency molybdenum phosphide (MoP) catalyst anchored to a porous nitrogen-doped carbon layer (MoP@NC-C_3N_4) via self-assembly and *in situ* phosphating processes with a clean phosphorus source (ammonium polyphosphate) and a pore-forming agent (F-108). The electrochemical test results demonstrate that the synthesized MoP@NC-C_3N_4 catalyst exhibits outstanding catalytic activity and durability in acidic and alkaline environments with overpotentials of 131 and 127 mV and Tafel slopes of 67 and 89 mV·dec^{-1} (10 mA·cm^{-2}), respectively. In the catalyst system, g-C_3N_4 provides both C and N atoms. In addition, the amorphous carbon and MoP nanoparticles exhibit a synergistic effect to promote charge transfer, thereby enhancing catalytic activity. The overpotential of MoP@NC-C_3N_4 in KOH electrolytes is lower than that of commercial Pt/C at current densities greater than 110 mA·cm^{-2}. This performance provides a valuable reference for potential industrial applications. The density functional theory results indicate that the Mo atom of MoP has the lowest hydrogen adsorption free energy and serves as the optimal catalytic active site for MoP@NC-C_3N_4. This study paves the way for the design and development of efficient HER electrocatalysts based on graphitic carbon nitrides (g-C_3N_4).

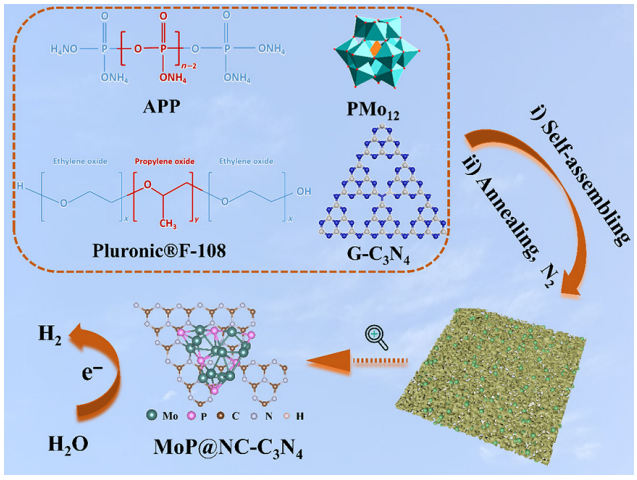

KEYWORDS: hydrogen evolution, graphitic carbon nitrides (g-C_3N_4), ammonium polyphosphate, synergistic effect, density functional theory (DFT)

1 Introduction

Hydrogen energy production is an effective approach for mitigating environmental pollution and the energy crisis. Hydrogen energy has received significant research attention because of its high calorific value for combustion and non-pollution [1–4]. Steam reforming is an efficient method for producing industrial hydrogen by reforming hydrocarbons, such as alkanes, to convert hydrocarbon vapors into hydrogen and carbon dioxide. However, although this method is highly efficient, it produces highly polluting gases such as carbon monoxide and carbon dioxide [5–7]. Consequently, the large-scale and efficient production of green hydrogen has become a global research topic. Water electrolysis is an effective approach for mitigating challenges associated with energy scarcity and environmental pollution, and it is expected to replace steam reforming for hydrogen production at a large scale [8–10].

In an actual hydrogen evolution reaction (HER), the cathode potential is less than the theoretical value due to electrode polarization, making HER difficult to perform. Furthermore, a greater overpotential is required to overcome this polarization effect. Therefore, developing catalysts that provide additional active sites and improve the reaction pathways is essential to reduce the overpotential and improve the efficiency of HER [11, 12]. Platinum (Pt)-based catalysts are among the most mature catalysts to date, with the adsorption of platinum to hydrogen intermediates being close to ideal values. However, the exorbitant price and scarcity of platinum limit the large-scale industrial production of Pt-based catalysts. Molybdenum-based hydrogen evolution catalysts are considered an ideal alternative to precious metal catalysts because of

Received: October 9, 2025; **Revised:** January 5, 2026
Accepted: January 10, 2026

✉Address correspondence to Xuejian Zhang, zxj_0620@163.com; Xiao Li, lix@cust.edu.cn; Zhongmin Su, zmsu@nenu.edu.cn

https://doi.org/10.26599/POM.2026.9140115

their advantages, such as a simple fabrication process, low cost, high catalytic activity, and strong stability [13]. Therefore, the research and development of low-cost, high-efficiency, and green HER catalysts are critical [13–17]. Current Mo-based hydrogen evolution catalysts incorporate transition metal compounds (carbides, nitrides, sulfides, phosphides, and borides), high-entropy alloys, etc. [18–24]. Among them, molybdenum phosphide (MoP) exhibits structural characteristics similar to those of natural hydrogenases and significant potential as efficient hydrogen evolution catalysts. However, if the Gibbs free energy (ΔG_{H^*}) of the active site of a MoP-based catalyst is close to 0, it is necessary to optimize the electronic structure of MoP to enhance the intrinsic catalytic properties of the catalyst [25, 26].

Based on the above analysis, many studies have demonstrated that graphitic carbon nitrides (g-C_3N_4), as a support or maskant, are crucial for enhancing the activity and durability of metal-based catalysts by electronically regulating the interface, and their stability is primarily attributed to the C–N covalent bond in g-C_3N_4. Moreover, the coupling of g-C_3N_4 to metals can enhance electron transport and thus electrocatalytic activity [12]. For example, Sajan et al. prepared g-C_3N_4/Ce-doped Fe_2O_3 heterostructures via hydrothermal synthesis, achieving an overpotential of 145 mV (10 mA·cm^{-2}) [27]. Wang et al. synthesized bimetallic sulfide anchoring by C_3N_4 walls for HER, achieving overpotentials of 164 and 95 mV in 0.5-M sulfuric acid and 1.0-M potassium hydroxide solutions, respectively [28].

In this study, we successfully synthesized MoP-based nanoparticles anchored on porous amorphous carbon (MoP@NC-C_3N_4). In this system, ammonium polyphosphate (APP) decomposes at high temperatures into phosphoric acid and ammonia gas, which can serve as both sources of nitrogen and phosphorus with an electrostatic attraction to PMo_{12}. The synthesized MoP@NC-C_3N_4 catalyst exhibits satisfactory catalytic activity and durable stability in both acidic and alkaline electrolytes. The use of g-C_3N_4 as a carbon source substrate reduces the agglomeration of MoP nanoparticles, exposing additional active sites. Moreover, density functional theory (DFT) calculations demonstrate that the Mo atoms in MoP are the optimal active sites in the MoP@NC-C_3N_4 catalyst and that N- and P-doped carbon layers synergize with MoP to achieve catalytic effects. This study has implications for the large-scale high-efficiency synthesis of hydrogen evolution catalysts.

2 Results and discussion

2.1 Characterization of catalyst

An efficient hydrogen evolution catalyst was prepared using self-assembly and the one-step calcination method, as shown in Scheme 1. F-108 was selected as the hard template during the preparation process. g-C_3N_4 serves as a rich source of both carbon and nitrogen for this system and interacts with F-108 (Figs. S1–S3 in the Electronic Supplementary Material (ESM)). During calcination, numerous mesoporous structures are created. Thermodynamic analysis reveals that g-C_3N_4 decomposes into amorphous carbon at a high-temperature calcination of 850 °C (Fig. S4 in the ESM). In addition, the infrared spectra of the synthesized catalyst show that the precursor exhibits the characteristic peak of g-C_3N_4 (1625 cm^{-1}, C=N). However, this characteristic peak is almost completely absent after the precursor is subjected to high-temperature calcination at 850 °C. This result demonstrates that g-C_3N_4 decomposes at 850 °C (Fig. S5 in the ESM). APP is selected as the phosphorus source and electrostatically interacts with PMo_{12} to synthesize MoP nanoparticles anchored to porous carbon [29]. g-C_3N_4, F-108, PMo_{12}, and APP were first synthesized as molybdenum-based precursors through a self-assembly process and then calcined at 350 °C in a nitrogen atmosphere for 1 h and at 850 °C for 2 h to obtain a hydrogen evolution catalyst (MoP@NC-C_3N_4). The obtained catalyst was then used to investigate hydrogen evolution in water electrolysis. F-108 was removed during the calcination process at 350 °C, leaving pores in the catalyst structure. Under APP induction, when the calcination temperature reached 850 °C, the catalyst was successfully phosphatized. Moreover, for comparison, a suite of contrast catalysts was synthesized using the same method, namely, Mo_2C@NC, MoP@NC, $Mo(PO_3)_3$, MoP@NC-MA, precursor, and PNC.

Powder X-ray diffraction (PXRD) was used to characterize the phase composition and crystallinity of the catalyst. The results are presented in Fig. 1(a), where MoP@NC-C_3N_4 is well crystalline and exhibits a MoP phase (PDF#24-0771). The peaks of MoP@NC-C_3N_4 are observed at 27.8°, 32.1°, 43.1°, 57.5°, 57.7°, 64.8°, 67.1°, 67.9°, and 74.3°, which correspond to the crystal planes of (001), (100), (101), (110), (002), (111), (200), (102), and (201), respectively. The diffraction patterns of the contrast catalysts (Mo_2C@NC, MoP@NC, $Mo(PO_3)_3$, and MoP@NC-MA) were analyzed to determine their phase compositions. Based on the PXRD pattern of Mo_2C@NC (JCPDS Card No.35-0787) (Fig. S6(a) in the ESM), the peaks at 34.4°, 37.9°, 39.4°, 52.1°, 61.5°, 69.6°, 72.4°, and 74.6° are primarily attributed to the (100), (002), (101), (102), (110), (103), (200), (112), and (201) crystal planes of Mo_2C, respectively. As shown in Figs. S6(b) and S6(d) in the ESM, the diffraction peaks in the PXRD patterns of MoP@NC and MoP@NC-MA are consistent with those of MoP (JCPDS Card No.24-0771), demonstrating that MoP@NC-MA and MoP@NC-C_3N_4 have the same phase, with the only difference being their carbon sources. The phase composition of $Mo(PO_3)_3$ was also analyzed. The PXRD diffraction peak pattern showed that the primary component was $Mo(PO_3)_3$ (JCPDS Card

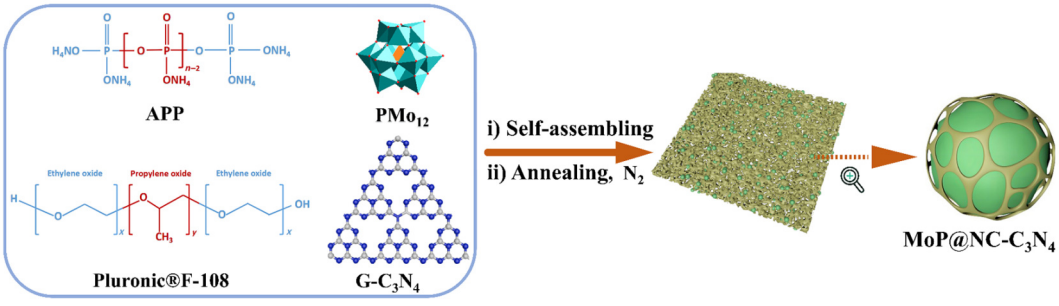

Scheme 1 Schematic diagram of MoP@NC-C_3N_4 synthesis.

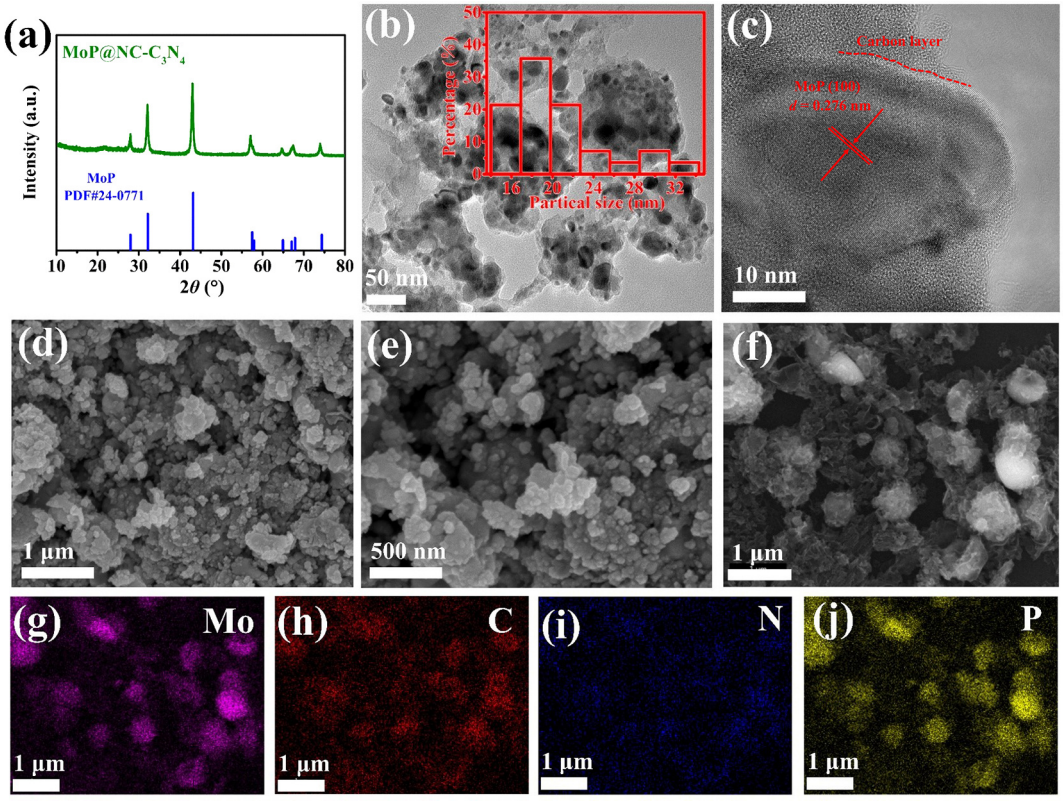

Figure 1 The characterization of the microstructure of MoP@NC-C_3N_4. (a) XRD pattern, (b) TEM image (inset: the particle size distribution image), (c) HRTEM image, (d) and (e) SEM images, (f)–(j) EDX mapping of Mo, C, N and P.

No.09-0106) (Fig. S6(c) in the ESM). The diffraction peaks are primarily located at 16.5° (031), 18.6° (002), 22.5° (141), 24.3° (150), 25.4° (310), 26.6° (202), 28.4° (222), 31.2° (213), 32.1° (123), 36.2° (080), and 43.7° (433). Without the addition of a carbon source, the oxygen atom in the precursor would form phosphorus- and molybdenum-containing compounds.

The microstructure of MoP@NC-C_3N_4 was characterized via transmission electron microscopy (TEM). As shown in Fig. 1(b), MoP@NC-C_3N_4 comprises spherical MoP nanoparticles with particle sizes ranging from 16 to 22 nm. According to the high-resolution TEM (HRTEM) image, only the lattice fringes of MoP nanoparticles exist in the catalyst and are encapsulated by graphite carbon, with a lattice spacing of 0.276 nm, which can be attributed to the (100) crystal plane of MoP (Fig. 1(c)). For comparison with MoP@NC-C_3N_4, scanning electron microscopy (SEM) and TEM images of MoP@NC-MA were also analyzed. Figure S7 in the ESM shows that MoP@NC-MA is composed of nanoparticles of different sizes (15–60 nm), which exhibit a certain degree of aggregation. The SEM images of MoP@NC-C_3N_4 (Figs. 1(d) and 1(e)) show that the catalyst comprises nanoparticles of nonuniform sizes. The energy-dispersive X-ray spectroscopy (EDX) images (Figs. 1(f)–1(j)) show that Mo, C, N, and P atoms exist in the catalyst and are uniformly distributed.

The degree of carbonization of the outer carbon shell of the catalyst was characterized and analyzed via Raman spectroscopy (Fig. S8 in the ESM). In the Raman spectrum of MoP@NC-C_3N_4, two strong peaks appear at 1353 and 1600 cm^{-1}, corresponding to the D and G bands of carbon, representing graphitic and amorphous carbon structures, respectively. The intensity ratio (I_D/I_G) of the D band to the G band was 0.894 (Fig. S8(a) in the ESM). As shown in Figs. S8(b)–S8(d) in the ESM, the I_D/I_G intensity ratios for MoP@NC-MA, MoP@NC, and Mo_2C@NC are 0.93, 0.932, and 0.97, respectively. This result indicates that MoP@NC-C_3N_4 exhibits a higher degree of graphitization than MoP@NC-MA, MoP@NC, and Mo_2C@NC, which enhances its electroconductivity.

N_2 adsorption–desorption isotherms and Brunauer–Emmett–Teller (BET) specific surface area analysis were used to investigate the pore structure and specific surface area of the synthesized catalyst. As shown in Fig. S9 in the ESM, the BET-specific surface area of MoP@NC-C_3N_4 is 180.3 $m^2 \cdot g^{-1}$ and displays an obvious H3-type hysteresis ring. The pore size distribution map shows that MoP@NC-C_3N_4 has two pore sizes of 1.7 and 2.05 nm, indicating that it has a microporous and mesoporous structure. Furthermore, the N_2 adsorption–desorption isotherms of the contrast catalysts MoP@NC and MoP@NC-MA were collected. The results are presented in Figs. S10 and S11 in the ESM. Without the addition of F-108, the specific surface area is only 12.1 $m^2 \cdot g^{-1}$, and the pore diameters are primarily concentrated at 2.24 nm, forming a mesoporous structure. This result confirms that F-108 addition facilitates the formation of porous structures. MoP@NC-MA exhibits a specific surface area of 114.6 m^2/g and a primary pore diameter of 2.34 nm, indicating a mesoporous structure. Its specific surface area is smaller than that of MoP@NC-C_3N_4. The difference in surface area can be attributed to a degree of particle aggregation.

The valence states and chemical compositions of the elements (C, N, P, and Mo) in MoP@NC-C_3N_4 were analyzed using X-ray photoelectron spectroscopy (XPS; Fig. 2). Figure 2(a) shows the Mo 3d spectrum of MoP@NC-C_3N_4 with peaks at 236.3 and 233.4 eV, which belong to Mo^{6+} $3d_{3/2}$ and Mo^{6+} $3d_{5/2}$, respectively. The peaks

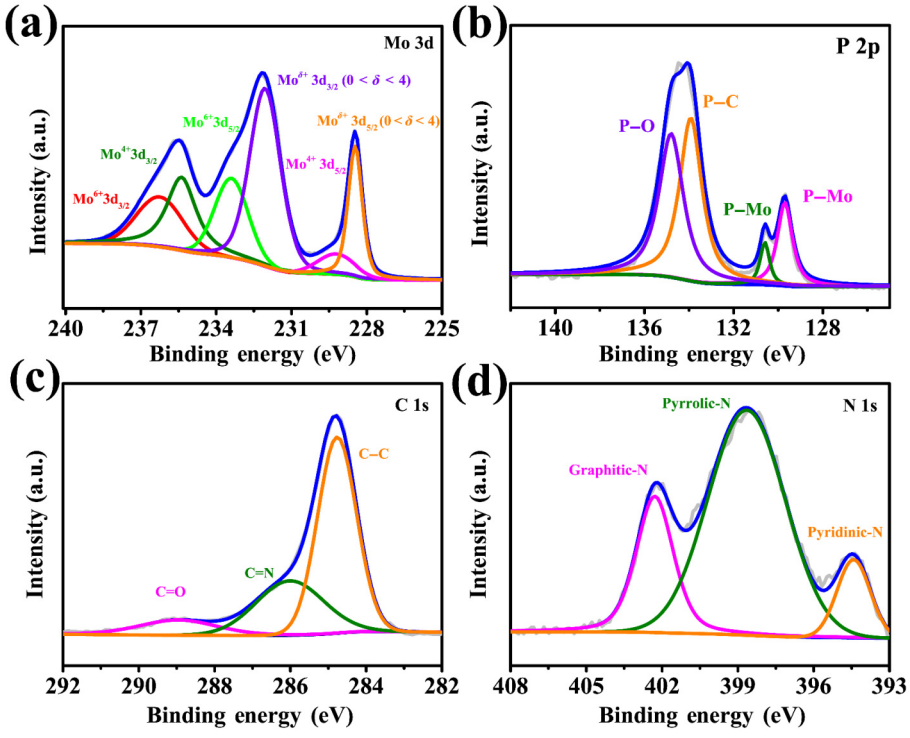

Figure 2 XPS spectra of (a) Mo 3d, (b) P 2p, (c) C 1s, and (d) N 1s of MoP@NC-C_3N_4.

located at 235.4 and 229.2 eV belong to Mo^{4+} $3d_{3/2}$ and Mo^{4+} $3d_{5/2}$, respectively. These peaks are attributed to the formation of molybdenum oxides, specifically MoO_3 and MoO_2 [30–32]. The other two peaks, located at 232.1 and 228.5 eV, belong to $Mo^{\delta+}$ ($0 < \delta < 4$), which can be attributed to the formation of Mo–P, which is the catalytic active center of HER [33]. The XPS spectrum of P 2p can be deconvoluted into three peaks: P–Mo (129.7 and 130.5 eV), P–C (133.9 eV), and P–O (134.8 eV) (Fig. 2(b)). The P–Mo bond at 129.7 and 130.5 eV demonstrates the successful formation of phosphides [34]. The XPS spectra of C 1s can be deconvoluted into three characteristic peaks (Fig. 2(c)): C–C (284.7 eV), C=N (286.0 eV), and C=O (289.0 eV) [35]. Moreover, the presence of the C=N bond indicates that the N atom is successfully doped into the carbon layer. As shown in Fig. 2(d), the N 1s spectra can be deconvoluted into graphitic-N (402.3 eV), pyrrolic-N (398.6 eV), and pyridinic-N (394.4 eV) [36].

For comparison, the XPS spectra of MoP@NC-MA were also analyzed. In Fig. S12(a) in the ESM, the peaks at 228.4 and 231.6 eV are assigned to $Mo^{\delta+}$ $3d_{5/2}$ ($0 < \delta < 4$) and $Mo^{\delta+}$ $3d_{3/2}$ ($0 < \delta < 4$), respectively, which can be attributed to the formation of Mo–P. This confirms the successful synthesis of MoP. The other two pairs of peaks (229.2 eV/236.1 eV and 233.3 eV/236.8 eV) can be ascribed to the formation of Mo^{4+} and Mo^{6+}, which correspond to MoO_2 and MoO_3, respectively [37]. The XPS spectrum of P 2p can be deconvoluted into four peaks at 129.6 eV/130.5 eV (P–Mo), 133.6 eV (P–C), and 134.6 eV (P–O), indicating the formation of the phosphide and confirming that the P atoms are doped into the graphite carbon (Fig. S12(b) in the ESM). In the C 1s XPS spectrum (Fig. S12(c) in the ESM), three peaks appear at 284.7, 285.9, and 288.3 eV, corresponding to C–C, C=N, and C=O, respectively. Similarly, in the N 1s XPS spectrum (Fig. S12(d) in the ESM), three peaks appear at 394.5 eV (pyridinic-N), 399.1 eV (pyrrolic-N), and 401.3 eV (graphitic-N).

2.2 Electrocatalytic HER performance

All catalysts, including the control catalysts, were subjected to electrochemical tests in acidic and alkaline environments. First, the synthesized catalyst was dispersed in ethanol, deionized water, and naphthol to obtain black ink, which was spread on the surface of a glassy carbon electrode and naturally dried at room temperature. Then, the electrode was activated at a scanning rate of 5 $mV \cdot s^{-1}$, and the polarization curve of the catalyst was obtained via linear sweep voltammetry (LSV). The carbonization temperature significantly influences the HER properties of the catalyst. The HER activity of MoP@NC-C_3N_4 at different calcination temperatures (600, 700, 750, 800, 850, 900, and 950 °C) is illustrated in Fig. S13 in the ESM. At a calcination temperature of 850 °C, the best HER performance is obtained, and the overpotential is the lowest in 0.5-M sulfuric acid and 1.0-M potassium hydroxide solutions. In addition, PXRD was applied to the catalyst at different pyrolysis temperatures. According to the obtained data, the crystalline phase of MoP (JCPDS Card No. 24-0771) begins to appear when the calcination temperature reaches 750 °C, which indicates the successful preparation of phosphide (Fig. S14 in the ESM). In addition to the calcination temperature, the content ratio of each component in the synthesized MoP@NC-C_3N_4 catalyst affects its HER activity. Therefore, the optimal mass ratios of the components (APP, PMo_{12}, g-C_3N_4, and F-108) in MoP@NC-C_3N_4 were investigated at a calcination temperature of 850 °C. As shown in Fig. S15 in the ESM, a comparison of the polarization curves indicates that the optimal HER performance of P@NC-C_3N_4 is achieved at a phosphomolybdic acid dosage of 80 mg, which corresponds to a mass ratio of phosphomolybdic acid to g-C_3N_4 of 1:6. Next, the effect of APP addition on HER performance was investigated (Fig. S16 in the ESM). The optimal mass ratio of APP to g-C_3N_4 is 1:5 in both acidic and alkaline environments. Finally, the dosage of surfactant F-108 was adjusted to achieve the best HER effect. The

polarization curve of the mass ratio of F-108 to APP in Fig. S17 in the ESM shows that the optimal ratio is 1:1, at which the F-108 addition is 100 mg. Based on the aforementioned proportions, MoP@NC-C_3N_4 was successfully prepared for subsequent electrochemical test experiments.

For a more comprehensive study of the electrochemical properties of MoP@NC-C_3N_4, the contrast catalysts MoP@NC-MA, Mo_2C@NC, MoP@NC, and $Mo(PO_3)_3$ were fabricated under the same conditions. Figure 3(a) shows that in 0.5-M sulfuric acid (10 mA·cm^{-2}), Pt/C exhibits a low overpotential of 10 mV and the best HER performance. MoP@NC-C_3N_4 also exhibits good HER activity with a low overpotential of 131 mV at a current density of 10 mA·cm^{-2}. Compared with the contrast catalysts MoP@NC-MA (164 mV), Mo_2C@NC (189 mV), MoP@NC (211 mV), and $Mo(PO_3)_3$ (368 mV), the synthesized MoP@NC-C_3N_4 catalyst exhibits superior catalytic activity, which is closely related to the successful doping of P and N atoms in the carbon layer and the unique porous structure of the catalyst. Moreover, the LSV curve of the precursor demonstrates that it exhibits no hydrogen evolution activity, indicating extremely poor conductivity, which is subsequently improved via high-temperature carbonization and phosphating. The sample also exhibits extremely poor catalytic activity in the absence of a metal source, further demonstrating the synergistic effect between MoP nanoparticles and the carbon layer (Fig. S18(a) in the ESM). The Tafel slope calculated from the LSV curve reflects the hydrodynamic evolution of the catalyst. As shown in Fig. 3(b), the Tafel slope of commercial Pt/C is 30 mV·dec^{-1}, whereas that of MoP@NC-C_3N_4 is 67 mV·dec^{-1}, demonstrating that the hydrogen evolution process of the synthesized catalyst is consistent with the Volmer–Heyrovsky mechanism. The Tafel slopes of the contrast catalysts MoP@NC-MA, Mo_2C@NC, MoP@NC, and $Mo(PO_3)_3$ were 92, 128, 96, and 156 mV·dec^{-1}, respectively. This result implies that their hydrogen evolution dynamics are slower than that of MoP@NC-C_3N_4. Cyclic voltammetry (CV) curves were obtained at different scanning rates (25–200 mV·s^{-1}) within a voltage range of −0.1–0.1 V (vs. RHE), as shown in Fig. 3(c) and Fig. S19 in the ESM . Thus, the double-layer capacitance (C_{dl}) value was calculated to compare the electrochemically active surface areas (ECSAs) of the catalysts. The C_{dl} values of MoP@NC-C_3N_4, MoP@NC-MA, Mo_2C@NC, MoP@NC, and $Mo(PO_3)_3$ were 50.49, 36.61, 28.74, 9.91, and 8.99 mF·cm^{-2}, respectively (Fig. 3(d)). MoP@NC-C_3N_4 exhibits the largest ECSA, which provides more active sites and improves its HER performance.

Electrochemical impedance spectroscopy (EIS) reflects the electron transfer behavior of a catalyst at the electrolyte interface,

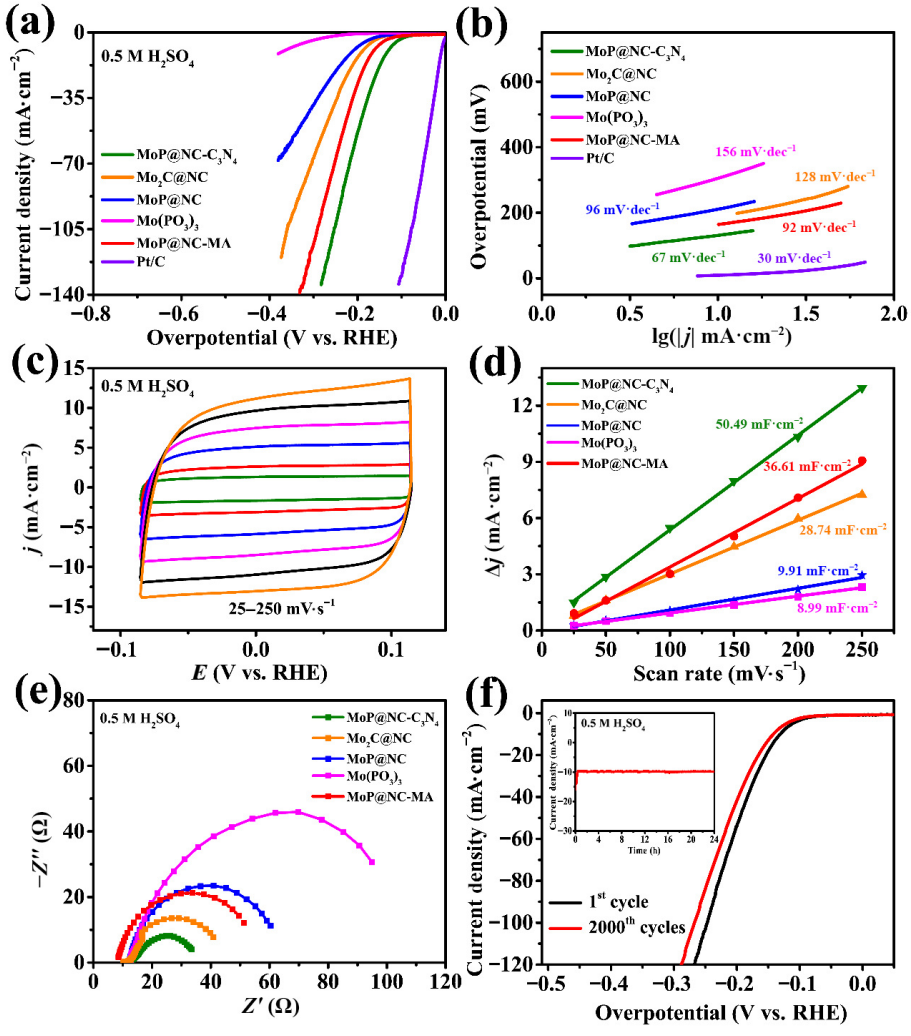

Figure 3 (a) LSV curves, (b) Tafel slope plots, (c) cyclic voltammetry curves, (d) C_{dl} values, (e) Nyquist plots, and (f) polarization curves (inset: time-dependent current density curve of MoP@NC-C_3N_4 (10 mA·cm^{-2}) for 24 h).

which is beneficial for evaluating its electrocatalytic performance. Figure 3(e) shows the Nyquist curves of MoP@NC-C_3N_4, Mo_2C@NC, MoP@NC, $Mo(PO_3)_3$, and MoP@NC-MA. Among them, MoP@NC-C_3N_4 exhibits the smallest Nyquist curve radius, indicating that it exhibits the lowest charge transfer resistance (R_{ct}) and highest charge transfer efficiency. Perdurability is also a vital indicator for determining the large-scale commercial applicability of a catalyst. As shown in Fig. 3(f), the LSV curve of MoP@NC-C_3N_4 does not change significantly after 2000 CV cycles in 0.5-M sulfuric acid, and the inset shows that the catalyst maintains good performance for 24 h. In addition, after the perdurability test, the catalyst was characterized by XRD, SEM, and TEM, and its properties were analyzed. As shown in Fig. S20 in the ESM, the XRD pattern indicates that the catalyst retains the MoP phase after testing, indicating that its structure has not changed. The SEM and TEM images indicate that the catalyst still exhibits a nonuniform nanoparticle state after the acid environment test, and the HRTEM image also shows that the spacing of the lattice stripes is 0.276 nm, which is consistent with that before the test. The EDX mapping images show that Mo, P, C, and N remain uniformly distributed throughout the catalyst. These results suggest that MoP@NC-C_3N_4 exhibits good stability.

In 1.0-M KOH, Pt/C exhibits the lowest overpotential (30 mV) and the smallest Tafel slope (47 mV dec^{-1}, 10 mA cm^{-2}). The overpotential and Tafel slopes of MoP@NC-C_3N_4 are 127 and 89 mV·dec^{-1}, respectively, which are significantly lower than those of MoP@NC-MA (176 mV), Mo_2C@NC (163 mV), MoP@NC (209 mV), and $Mo(PO_3)_3$ (299 mV) (Figs. 4(a) and 4(b)). Similarly, the precursor and PNC exhibit extremely poor hydrogen evolution activity under alkaline conditions (Fig. S18(b) in the ESM). Under alkaline conditions, the high-temperature calcination process enhanced the conductivity of the catalyst and the synergistic effect between MoP and the amorphous carbon layer, thereby improving the catalytic activity of the catalyst. Figure 4(c) and Fig. S21 in the ESM show the CV curves of the catalysts. The C_{dl} values of MoP@NC-C_3N_4, MoP@NC-MA, Mo_2C@NC, MoP@NC, and $Mo(PO_3)_3$ were 22.17, 15.85, 19.01, 17.08, and 5.89 mF·cm^{-2}, respectively. These results demonstrate that MoP@NC-C_3N_4 has a large electrochemical surface area and can expose more active sites to enhance HER activity in alkaline environments (Fig. 4(d)). EIS was applied to the catalysts under an overpotential of 180 mV. Among all catalysts, MoP@NC-C_3N_4 exhibits the smallest semicircle radius in its Nyquist plot (Fig. 4(e)), demonstrating its low impedance and superior electrical conductivity. The excellent durability of the MoP@NC-C_3N_4 catalyst is indicated by the minimal change in its LSV curves after 2000 CV cycles and its

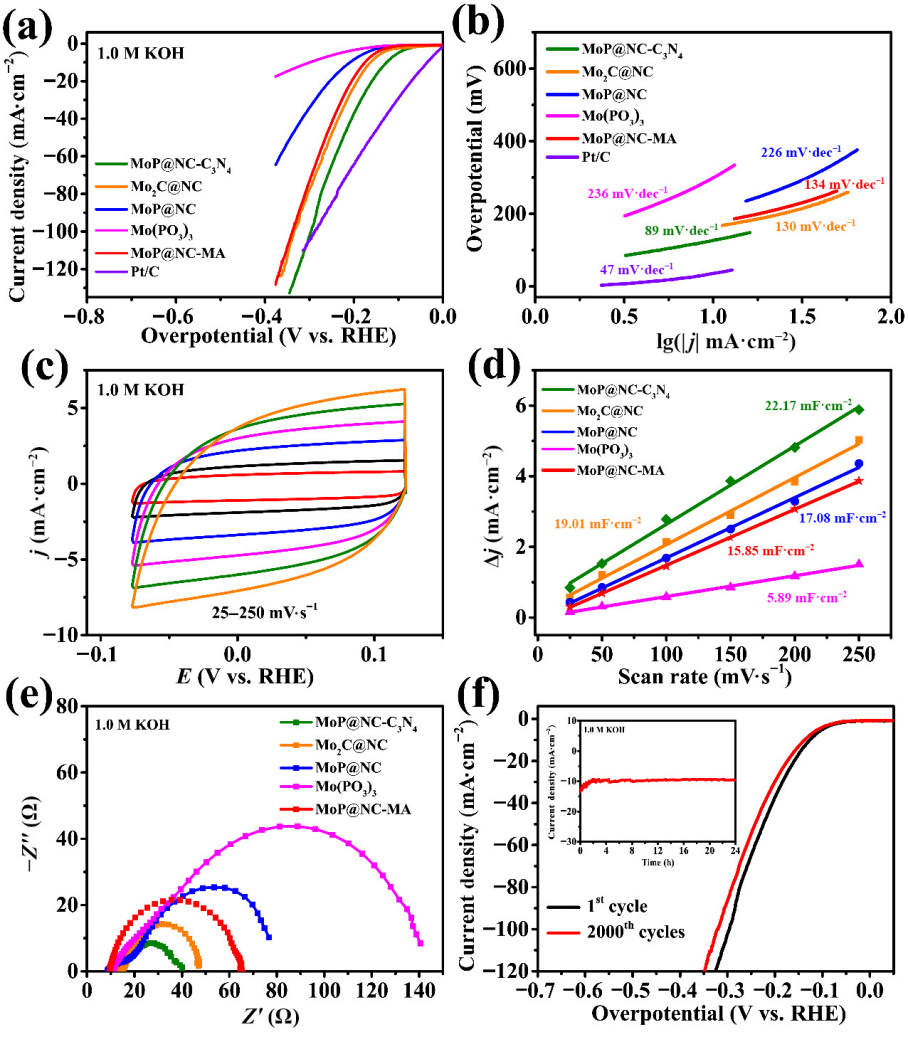

Figure 4 (a) Polarization curves, (b) Tafel slope plots, (c) cyclic voltammetry curves, (d) C_{dl} values, (e) Nyquist plots, and (f) polarization curves (Inset: time-dependent current density curve of MoP@NC-C_3N_4 (10 mA·cm^{-2}) for 24 h).

stable 24-h performance in the current–time (*i*–*t*) test (Fig. 4(f), inset). As previously mentioned, the XRD patterns, SEM images, and TEM images of the catalyst after testing in alkaline electrolytes were also analyzed (Fig. S22 in the ESM). The phase of the catalyst remains the same (i.e., MoP) as before the test. The SEM, TEM, and HRTEM images show that the synthesized catalyst comprises MoP nanoparticles. The EDX mapping images obtained after the test show that Mo, P, C, and N are uniformly distributed in the catalyst. In addition, the catalytic performance of recently reported transition metal MoP electrocatalysts is summarized in Table S1 in the ESM. Compared with these electrocatalysts, MoP@NC-C_3N_4 exhibits satisfactory hydrogen evolution performance.

2.3 DFT calculations

To further investigate the active site of the synthesized catalyst, DFT analysis was performed. The calculation details are presented in the ESM. First, the MoP nanoparticle-anchored nitrogen-doped carbon layer structure model was constructed based on the XRD pattern and HRTEM image of MoP. A unit cell with specific crystal faces of MoP (100) was selected for analysis (Fig. S23 in the ESM). Hydrogen adsorption Gibbs free energy (ΔG_{H^*}) is the most intuitive indicator for evaluating the performance of hydrogen evolution. In the hydrogen production reaction, the closer the ΔG_{H^*} is to 0, the easier it is for H* to undergo desorption and the faster the kinetic velocity [29]. The calculation results are presented in Fig. 5. The absolute value of the ΔG_{H^*} of the Mo atom is closest to 0, proving that the Mo atom is the optimal active site for hydrogen evolution (Fig. 5(a)). To verify the synergistic effect between MoP and the carbon layers, ΔG_{H^*} values were calculated for the N- and P-doped carbon layers. The results are presented in Fig. 5(b). The ΔG_{H^*} value of P doping on the carbon layer was the lowest, confirming that P atom doping accelerates the hydrogen adsorption process of the catalyst. Furthermore, the active sites are clarified by calculating the difference in charge density of the catalyst (Fig. 5). The yellow and cyan areas in Figs. 5(c) and 5(d) represent charge accumulation and depletion, respectively. The charge density aggregation is primarily concentrated on the hydrogen atoms of MoP, demonstrating that the H atoms bound to the Mo atoms are highly active and favorable sites for HER.

3 Conclusions

Single-metal phosphide (MoP) was successfully prepared via *in situ* phosphorylation and one-step calcination processes and anchored to a porous carbon layer for efficient HER. The synthesized MoP@NC-C_3N_4 catalyst exhibited low overpotentials (131 and 127 mV, respectively) and good durability in H_2SO_4 and KOH solutions (10 mA·cm^{-2}). Notably, in a 1.0-M KOH solution, the overpotential of the catalyst is lower than that of commercial Pt/C at a current density of 100 mA·cm^{-2}, which also demonstrates the advantage of the synthesized catalyst at high current densities. Electrochemical tests and DFT calculations demonstrate that the Mo atom of MoP is the optimal active site for hydrogen evolution, thereby enhancing the hydrogen evolution performance of the synthesized catalyst. Furthermore, the porous structure exposes abundant active sites, accelerating the charge transfer rate. The synergistic effect of MoP nanoparticles and carbon layers enhances the catalytic activity of the synthesized catalyst, thereby accelerating the adsorption–desorption process of H atoms and reducing the catalytic overpotential. This study sheds new light on the large-scale industrial production of hydrogen evolution catalysts.

Electronic Supplementary Material: Supplementary material (experiment section, DFT calculations, XRD pattern, Raman spectroscopy, XPS spectra, LSV cruves, CV curves, SEM and TEM images, schematic diagrams of unit cell structure for MoP) is

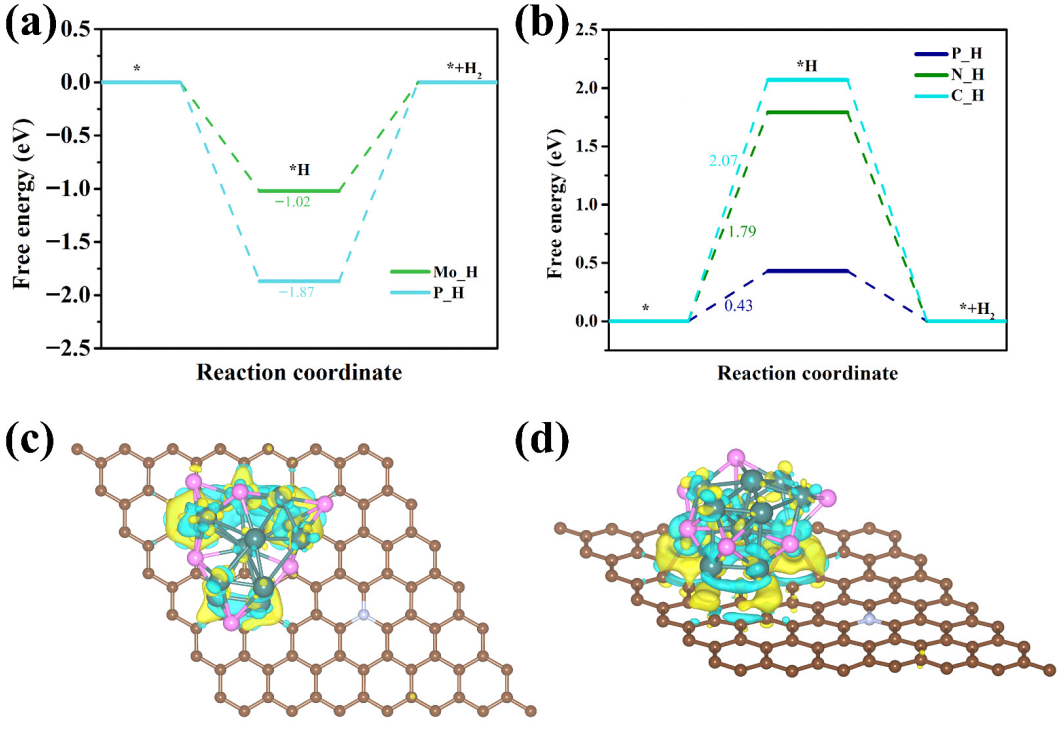

Figure 5 (a) ΔG_{H^*} of MoP (100) and (b) ΔG_{H^*} of N and P doped carbon layer, (c) the charge density difference ($\Delta\rho$) with the cyan and yellow areas showing low and high charge density, respectively and (d) the charge density difference ($\Delta\rho$) of front view.

available in the online version of this article at https://doi.org/10.26599/POM.2026.9140115.

Data availability

All data needed to support the conclusions in the paper are presented in the manuscript and the Electronic Supplementary Material. Additional data related to this paper may be requested from the corresponding author upon request.

Acknowledgments

This work was financially supported by Joint Fund Project of the Natural Science Foundation of jilin Province (No. YDZJ202301ZYTS290) and Education Scientific Research Project of Jilin Provincial Department (Nos. JJKH20240359KJ and JJKH20240358KJ).

Declaration of competing interest

The authors declare that they have no known competing financial interests or personal relationships that could have appeared to influence the work reported in this paper. Author Zhongmin Su is the advisory board member of this journal, but he is not involved in the peer-review or decision of this article.

Author contribution statement

J. L.: Data curation, writing – review & editing. Z. N. L: Software, formal analysis. C. W. W: Writing – original draft, software. T. C. S: Data curation, methodology, investigation. X. J. Z.: Formal analysis, conceptualization. X. L.: Funding acquisition, investigation. H. S. L.: Writing – original draft. Y. T. L.: Validation, supervision, formal analysis. Z. M. S.: Funding acquisition, project administration.

Use of AI statement

None.

References

[1] Shen, F. Y.; Zhang, Z. H.; Wang, Z.; Ren, H.; Liang, X. H.; Cai, Z. J.; Yang, S. T.; Sun, G. D.; Cao, Y. N.; Yang, X. X. et al. Oxophilic Ce single atoms-triggered active sites reverse for superior alkaline hydrogen evolution. *Nat. Commun.* **2024**, *15*, 448.

[2] Du, J. J.; Zhou, Y.; Liu, X. H.; Cui, X. X.; Zhang, X.; Wang, B.; Feng, X.; Zhu, J.; Zuo, H.; Li, Q. et al. Rational design of porous vanadium-based alloys modified with a Ni–Cu–Mo coating for alkaline water electrolysis. *Electrochim. Acta* **2024**, *499*, 144676.

[3] Wu, W. Y.; Zhai, H. B.; Holubnyak, E. Technological evolution of large-scale blue hydrogen production toward the U.S. Hydrogen Energy Earthshot. *Nat. Commun.* **2024**, *15*, 5684.

[4] Liu, Y. H.; Chen, Q. B.; An, Y. K.; Qiu, H. L.; Ma, S. H.; Liu, H. J.; Hu, Z. G.; Wu, Y. C. Electrocatalytic hydrogen evolution and doping modification of Weyl semimetal $PtBi_2$ acidic solutions. *Inorg. Chem. Front.* **2025**, *12*, 3217–3228.

[5] Alhassan, M.; Jalil, A. A.; Owgi, A. H. K.; Hamid, M. Y. S.; Bahari, M. B.; van Tran, T.; Nabgan, W.; Hatta, A. H.; Khusnun, N. F. B.; Amusa, A. A. et al. Emerging trends in hydrogen and synfuel generation: A state-of-the-art review. *Environ. Sci. Pollut. Res.* **2024**, *31*, 42640–42671.

[6] Su, Q. B.; Li, C.; Ren, H. J.; Yan, Y. C.; Li, J. Study of the performance of hydrogen production by autothermal steam reforming as dimethyl ether in a fan-shaped channel reactor. *J. Energy Eng.* **2025**, *151*, 04024043.

[7] Wang, Y. L.; Su, B. S.; Yang, X. Y.; Chen, Z. Q.; Wang, S. A green hydrogen production system based on solar-assisted biogas steam reforming. *Appl. Therm. Eng.* **2024**, *248*, 123067.

[8] Sun, M. W.; Zhang, N. Electronic structure engineering of transition-metal-based electrocatalysts for water splitting. *ACS Sustain. Chem. Eng.* **2024**, *12*, 15788–15811.

[9] Chen, Y. X.; Zhao, X. H.; Dong, P.; Zhang, Y. J.; Zou, Y. Q.; Wang, S. Y. Carbon-based electrocatalysts for water splitting at high-current-densities: A review. *New Carbon Mater.* **2024**, *39*, 1–16.

[10] He, Y. J.; Liu, W.; Liu, J. Q. MOF-based/derived catalysts for electrochemical overall water splitting. *J. Colloid Interface Sci.* **2024**, *661*, 409–435.

[11] Jeghan, S. M. N.; Seo, B.; Son, H.; Joo, S. W.; Kim, M. K.; Lee, G. Exfoliated defects-rich g-C_3N_4 nanosheets heterointerface engineering with $CuCo_2O_4$ as promising bifunctional electrocatalysts for seawater splitting. *Chem. Eng. J.* **2024**, *487*, 150576.

[12] Zhang, B. Y.; Li, J. Q.; Song, Q. Q.; Lv, S. Y.; Shi, Y. L.; Liu, H. g-C_3N_4-modulated bifunctional SnO_2@g-C_3N_4@SnS_2 hollow nanospheres for efficient electrochemical overall water splitting. *Appl. Surf. Sci.* **2022**, *589*, 153016.

[13] Tang, Y. J.; Gao, M. R.; Liu, C. H.; Li, S. L.; Jiang, H. L.; Lan, Y. Q.; Han, M.; Yu, S. H. Porous molybdenum-based hybrid catalysts for highly efficient hydrogen evolution. *Angew. Chem., Int. Ed.* **2015**, *54*, 12928–12932.

[14] Lou, H.; Ma, C. Metallic PtC monolayer as a promising hydrogen evolution electrocatalyst. *Phys. Chem. Chem. Phys.* **2025**, *27*, 2749–2757.

[15] Lv, J. Q.; Li, B.; Liu, Q. Q.; Gao, Z. X.; Lang, Z. L.; Liang, S.; Li, Y. Q.; Zang, H. Y. Designed tetranuclear iron-oxo clusters with redox activity for high-performance lithium storage. *Angew. Chem., Int. Ed.* **2023**, *62*, e202306193.

[16] Cheng, S. H.; Lang, Z. L.; Du, J.; Du, Z. L.; Li, Y. Q.; Tan, H. Q.; Li, Y. G. Engineering of iridium complexes for the efficient hydrogen evolution of formic acid without additives. *J Catal.* **2022**, *413*, 119–126.

[17] Salah, A.; Ren, H. D.; Al-Ansi, N.; Tan, H. Q.; Yu, F. Y.; Liu, Y. C.; Thamer, B. M.; Al-Salihy, A.; Zhao, L.; Li, Y. G. Dispersing small Ru nanoparticles into boron nitride remodified by reduced graphene oxide for high-efficient electrocatalytic hydrogen evolution reaction. *J. Colloid Interface Sci.* **2023**, *644*, 378–387.

[18] Oh, Y.; Theerthagiri, J.; Min, A.; Moon, C. J.; Yu, Y.; Choi, M. Y. Pulsed laser interference patterning of transition-metal carbides for stable alkaline water electrolysis kinetics. *Carbon Energy* **2024**, *6*, e448.

[19] Zhou, P. F.; Liu, X. C.; Ge, X.; Feng, J. X. *In situ* generated α-$Co(OH)_2$/Co_3Mo derived from Co–Mo–N for enhanced electrochemical hydrogen evolution reaction. *J. Mater. Chem. A* **2024**, *12*, 32775–32782.

[20] Zhao, J. J.; Huang, Z.; Zhou, L. W.; Kuang, S. F.; Pi, Z. G.; Lin, H.; Nie, M.; Li, Q. Formation of GO supported CoS_2@MoS_2 heterostructures with efficient electrocatalysis for water splitting. *Chem. Phys. Lett.* **2024**, *841*, 141195.

[21] Zhang, T.; Zhong, J. G.; Gao, W.; Wang, Y. X. Interface engineering induced N, P-doped carbon-shell-encapsulated FeP/NiP_2/Ni_5P_4/NiP nanoparticles for highly efficient hydrogen evolution reaction. *Coatings* **2024**, *14*, 817.

[22] Xu, N.; Li, X. R.; Ouyang, D. H.; Li, G. D.; Cheng, S. J.; Tang, Z. M.; Chai, Y. M.; Dong, B. Structural and electronic regulation of transition metal borides: From controllable synthesis to industrial alkaline water splitting. *Fuel* **2025**, *386*, 134283.

[23] Wang, Z. D.; Xia, T.; Li, Z. H.; Shao, M. F. A review of carbon-based catalysts and catalyst supports for simultaneous organic electro-oxidation and hydrogen evolution reactions. *New Carbon Mater.* **2024**, *39*, 67–77.

[24] Gu, T.; Yu, F. S.; Yu, Z. Q.; Qi, Y. X.; Li, Y. X.; Miao, F.; Yan, Z. J.

Efficient dual-phase PtNiCuMnMo high-entropy alloy electrocatalyst for alkaline hydrogen evolution reaction. *J. Colloid Interface Sci.* **2025**, *688*, 308–316.
[25] Ji, L. L.; Wei, Y. J.; Wu, P. R.; Xu, M. Z.; Wang, T.; Wang, S.; Liang, Q. F.; Meyer, T. J.; Chen, Z. F. Heterointerface engineering of Ni_2P–Co_2P nanoframes for efficient water splitting. *Chem. Mater.* **2021**, *33*, 9165–9173.
[26] Lang, Z. L.; Miao, J.; Tan, H. Q.; Su, Z. M.; Li, Y. G.; Zheng, Z. P. Element table of TM-substituted polyoxotungstates for direct electrocatalytic reduction of nitric oxide to ammonia: A DFT guideline for experiments. *Inorg. Chem. Front.* **2020**, *7*, 4507–4516.
[27] Anjana, R.; Hanamantrao, D. P.; Banu, G. N.; Raja, V.; Rimal Isaac, R. S.; John, J. S.; Vediappan, K.; Jose, S. P.; Neppolian, B.; Sajan, D. Hydrothermal synthesis of graphitic carbon nitride/Ce doped Fe_2O_3 heterostructures for supercapattery device and hydrogen evolution reaction. *J Energy Storage* **2025**, *116*, 116021.
[28] Wang, Y. Q.; Wang, T.; Xu, M.; Li, B. W.; Gao, Z.; Zhang, W. J.; Li, Z. X.; Qu, C. Q.; Feng, M. Polyoxometalate superlattices derived bimetallic sulfides to accelerate acidic and alkaline hydrogen evolution reaction. *J. Colloid Interface Sci.* **2025**, *679*, 760–768.
[29] Li, J.; Liu, Y.; Li, X.; Pan, Q. Q.; Sun, D.; Men, L. L.; Sun, B.; Xu, C. Y.; Su, Z. M. Ammonium polyphosphate induced bimetallic phosphides nanoparticles coated with porous N-doped carbon for efficiently electrochemical hydrogen evolution. *Chem. Eng. J.* **2022**, *431*, 133696.
[30] Ma, H.; Yan, W. S.; Yu, Y. L.; Deng, L. H.; Hong, Z.; Song, L.; Li, L. Phosphorus vacancies improve the hydrogen evolution of MoP electrocatalysts. *Nanoscale* **2023**, *15*, 1357–1364.
[31] Ji, Q. H.; Li, Z. Q.; Su, L. X.; Boateng, I. D.; Zhou, C. S. Preparation of sugarcane bagasse carbon-coated molybdenum phosphide nanocomposite electrocatalyst for hydrogen evolution reaction. *J Electroanal. Chem.* **2024**, *968*, 118513.
[32] Bhandari, G.; Dhakal, P. P.; Tran, D. T.; Nguyen, T. H.; Dinh, V. A.; Kim, N. H.; Lee, J. H. Pt single atom-doped triphasic VP-Ni_3P–MoP heterostructure: Unveiling a breakthrough electrocatalyst for efficient water splitting. *Small* **2024**, *20*, 2405952.
[33] Attarzadeh, N.; Lakshmi-Narayana, A.; Das, D.; Tan, S. H.; Shutthanandan, V.; Ramana, C. V. One-Step synthesis and operando electrochemical impedance spectroscopic characterization of heterostructured MoP–Mo_2N electrocatalysts for stable hydrogen evolution reaction. *ACS Appl. Mater. Interfaces* **2024**, *16*, 6958–6970.
[34] Pu, Z. H.; Wei, S. Y.; Chen, Z. B.; Mu, S. C. Flexible molybdenum phosphide nanosheet array electrodes for hydrogen evolution reaction in a wide pH range. *Appl. Catal. B Environ.* **2016**, *196*, 193–198.
[35] Zhang, X.; Yu, X. L.; Zhang, L. J.; Zhou, F.; Liang, Y. Y.; Wang, R. H. Molybdenum phosphide/carbon nanotube hybrids as PH-universal electrocatalysts for hydrogen evolution reaction. *Adv. Funct. Mater.* **2018**, *28*, 1706523.
[36] Zheng, W. R.; Liu, M. J.; Lee. L. Y. S. Best practices in using foam-type electrodes for electrocatalytic performance benchmark. *ACS Energy Lett.* **2020**, *5*, 3260–3264.
[37] Chen, Y. H.; Yue, K. H.; Zhao, J. W.; Cai, Z. Y.; Wang, X. Y.; Yan. Y. Effective modulating of the Mo dissolution and polymerization in $Ni_4Mo/NiMoO_4$ heterostructure via metal-metal oxide-support interaction for boosting H_2 production. *Chem. Eng. J.* **2023**, *466*, 143097.

Xiao Li, associate professor and master's supervisor, holds a doctoral degree from Northeast Normal University. Currently, she works at the College of Chemistry and Environmental Engineering of Changchun University of Science and Technology. Currently, she has been engaged in the synthesis of metal-organic framework (MOFs) materials and multi-acid (POM) composite materials, and conducting research on their applications, including: (1) carbon-coated multi-component materials derived from bimetallic MOFs and POM@MOFs for electrochemical water splitting; (2) synthesis and degradation of multifunctional MOFs and MOFs composites for dyes, fluorescence sensing, and ion adsorption properties research.

Zhongmin Su, Professor, Doctoral Supervisor, at Jilin University. He actively conducts research integrating experiments and theories in the fields of "Applied Quantum Chemistry" and "Functional Materials Chemistry". The main research directions include: the design and synthesis of metal-oxygen cluster (POM) compounds and their functional metal-organic framework (MOF) materials; the synthesis and application of organic optoelectronic materials and the theoretical research on their electronic transport properties; the study of the structural properties of new functional nanomaterials, etc. He is dedicated to the targeted structural design and synthesis of new systems of polyoxometalate compounds (POM) and functional metal-organic frameworks (MOF), as well as the research on functional properties such as photoelectricity, chirality, and catalysis. And he is Member of the Senior Talent Program of the Ministry of Education and member of the Chemistry Discipline Evaluation Committee of the Sixth and Seventh Sessions of the State Council Academic Degrees Committee.